DOI: 10.24874/ti.2122.01.25.02

Tribology in Industry

www.tribology.rs

RESEARCH

Influence of Tin Content on the Correlation Between Thermal Solidification Parameters, Macrostructure, and Machinability of Al-Sn Alloys Using the Surface Roughness Criterion

Gabriel Gomes[a,*], Jacson Nascimento[a], Athus Igor Castro Holanda [a], André Cruz da Costa Maciel[a], Héricles Ruiliman Oliveira de Souza [a], Amanda Lucena de Medeiros[a], Adrina Silva[a]

[a]*Faculty of Mechanical Engineering, Federal University of Pará, Augusto Corrêa Street, 01 - Guamá, Belém - PA, 66075-110, Pará, Brazil.*

Keywords:

Directional solidification
Low-miscibility alloys
Surface integrity
Machining performance
Plumose grains
Feathery grains
Constitutional undercooling

* Corresponding author:

Gabriel Gomes
E-mail: gabriel.gomes@itec.ufpa.br

Received: 23 December 2025
Revised: 29 January 2026
Accepted: 19 February 2026

A B S T R A C T

The machinability of aluminum-tin (Al-Sn) alloys is strongly influenced by solidification history, although solidification behavior and machining performance are often addressed independently. This study investigates the influence of tin content on the relationship between thermal solidification parameters, macrostructural evolution, and machining response of directionally solidified Al-Sn alloys. Al-10wt.%Sn and Al-20wt.%Sn alloys were solidified under identical transient heat extraction conditions, and liquidus isotherm velocity (V_L) and cooling rate ($\dot{T}$) were correlated with macrostructure and surface roughness after machining. Distinct macrostructural morphologies were obtained, with the Al-10wt.%Sn alloy exhibiting columnar, plumose, and equiaxial grains along the ingot length, whereas the higher Sn content promoted a predominantly equiaxial structure due to enhanced constitutional undercooling. Machinability was assessed by average surface roughness (Ra), measured using a non-contact optical method, with Ra values ranging from approximately 10.9 to 12.4 μm, depending on the macrostructural region. The results show that surface roughness is governed primarily by macrostructural morphology rather than alloy composition alone. Plumose and transition regions, typically located around P = 20 mm and P = 60 mm from the chilled surface, presented inferior surface finish (Ra ≈ 12.3-12.4 μm), whereas equiaxial regions exhibited lower and more homogeneous roughness levels (Ra ≈ 10.9 μm). Higher V_L and $\dot{T}$ conditions, which favor equiaxial grain formation, were consistently associated with improved machining response. These comparative findings provide a physically grounded framework linking solidification parameters, macrostructure, and machining response, supporting the development of machinability databases based on controlled solidification.

1. INTRODUCTION

Aluminum-tin (Al-Sn) alloys are widely used in antifriction components, bearings, and systems subjected to continuous relative motion, where low friction and high lubricant retention are required. The presence of tin-rich phases, practically immiscible in the aluminum matrix, confers self-lubricating characteristics to these alloys, making them attractive for tribological applications in automotive, aerospace, and mechanical systems [1-3].

From a metallurgical perspective, the extremely low solubility of Sn in aluminum leads to pronounced solute segregation during solidification, promoting heterogeneous microstructures with Sn-rich regions concentrated in interdendritic areas. This heterogeneity directly affects mechanical behavior, heat transfer, and deformation mechanisms during machining, rendering the final properties of Al-Sn alloys highly sensitive to solidification conditions [4-6].

Directional solidification under transient heat extraction enables systematic control of thermal parameters such as liquidus isotherm velocity (V_L) and cooling rate ($\dot{T}$), which govern macrostructural evolution, including the formation of columnar, plumose (feathery), and equiaxed grain morphologies [6-9]. Variations in these parameters influence solute redistribution, constitutional undercooling, and grain morphology, establishing a direct link between solidification kinetics and structural heterogeneity [10].

Machinability is not an intrinsic material property but results from interactions between cutting conditions and the microstructural features of the workpiece [11,12]. In Al-Sn alloys, microstructural heterogeneity associated with solute segregation and macrostructural transitions can significantly affect chip formation, local plastic deformation, heat generation, and surface integrity. In this context, surface roughness represents a practical and sensitive criterion for assessing machining response, as it reflects the combined effects of these mechanisms [13,14].

Despite the recognized influence of microstructure on machinability, important gaps remain in the literature [15]. Most studies address either solidification behavior or machining performance independently, often focusing on a single alloy composition and neglecting the combined role of thermal solidification parameters, macrostructural morphology, and machining response. Moreover, systematic comparisons between different Sn contents solidified under identical thermal conditions are scarce, limiting the development of consistent correlations between processing conditions and machinability outcomes [14,16,17].

Therefore, the present work investigates the influence of tin content (10wt.% and 20wt.%) on thermal solidification parameters (V_L and $\dot{T}$), macrostructural evolution, and machining response of directionally solidified Al-Sn alloys. Machinability is intentionally evaluated exclusively through the average surface roughness parameter as a comparative indicator under controlled conditions. By maintaining identical solidification and machining parameters for both compositions and performing spatially resolved machining along the ingot length, the study aims to identify physically consistent comparative trends while explicitly acknowledging the methodological limitations of the experimental design.

2. MATERIALS AND METHODS

2.1 Alloy preparation and thermal analysis

The Al-10wt.%Sn and Al-20wt.%Sn alloys were prepared based on rigorous stoichiometric calculations, considering both the effective mold volume and the useful capacity of the silicon carbide crucible. Commercially pure aluminum and tin were sectioned into small pieces using a cooled circular band saw to minimize oxidation and then weighed on an electronic balance with 0.01 g precision [14,18,19].

Melting was carried out in a resistance-heated muffle furnace using a silicon carbide crucible internally coated with refractory alumina to prevent contamination. Aluminum was initially melted, followed by the addition of solid tin, taking into account the significant difference between their melting temperatures. After complete melting, the alloy was reheated slightly

above its liquidus temperature and manually stirred using an alumina-coated stainless-steel spatula to ensure chemical homogeneity. The crucible was then sealed with an insulating ceramic cover to minimize heat losses during thermal analysis [18].

A calibrated K-type thermocouple was inserted into the melt to record the cooling curve in real time using a multichannel data acquisition system. The liquidus (T_L) and solidus (T_S) temperatures were determined from the cooling curves and compared with equilibrium values obtained from Thermo-Calc® simulations, confirming the nominal alloy compositions [18]. Fig. 1 shows the preparation of alloys for thermal analysis.

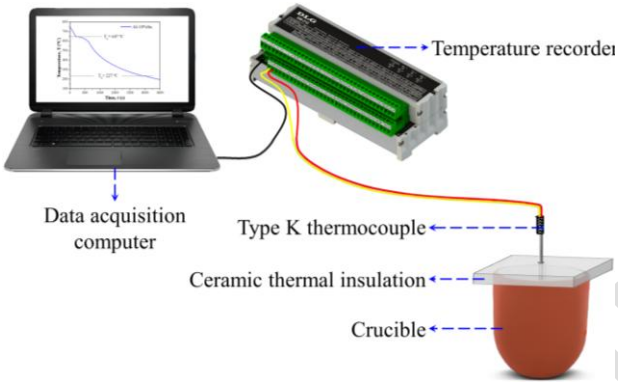

Fig. 1. Experimental setup for alloy preparation and cooling curve acquisition.

The experimental methodology employed in this study is well established in the literature and has been successfully applied in previous investigations involving Al-Sn alloys and similar metallic systems [14,19]. The procedures for alloy preparation, thermal analysis, and validation through comparison with Thermo-Calc® equilibrium simulations have been demonstrated to be reliable and reproducible, as evidenced by earlier works, thereby ensuring the technical consistency and scientific robustness of the present approach [18].

2.2 Directional solidification procedure

After thermal characterization, the alloys were remelted and directionally solidified using a horizontal solidification device designed to promote unidirectional heat extraction under transient conditions. The mold was equipped with longitudinally aligned K-type thermocouples positioned along the solidification direction to continuously record temperature evolution [18].

Before pouring, the mold was preheated above the liquidus temperature to ensure complete filling. Once the melt reached a superheat level of approximately 10% above T_L, the heating system was switched off and forced water cooling was activated on the external surface of the mold, inducing directional solidification from the cooled surface toward the opposite end of the ingot [18].

The thermal profiles obtained during solidification were used to calculate the V_L and $\dot{T}$ as functions of position along the ingot, following established analytical procedures reported in the literature [18,19].

2.3 Macrostructural characterization

After complete solidification, the ingots were removed from the mold and sectioned longitudinally along the solidification direction. Metallographic preparation followed ASTM E3 [20] standards, including cutting, grinding, polishing, and chemical etching [14,18,19].

Macrostructural features were revealed using Keller's reagent, allowing clear identification of columnar, plumose (feathery), and equiaxed grain regions. Macrographs were acquired using a high-resolution imaging system and analyzed to support qualitative and quantitative correlations between macrostructural morphology and the thermal solidification parameters V_L and $\dot{T}$ [14,18,19].

2.4 Machining tests

Machining tests were performed directly on the as-solidified ingots to preserve the microstructural gradient generated during directional solidification. No prior machining or geometric modification was applied to avoid metallurgical transformations, residual stresses, or microstructural alterations [14,19].

Dry parting-off (cut-off turning) operations were conducted along the longitudinal face of the ingots using a MANROD MR-320 bench lathe (Fig. 2) [21]. High-speed steel (HSS T6, ¾") cutting tools with factory-ground edges were employed to ensure consistent tool geometry. Cutting parameters were kept constant for all tests: spindle speed of 650 rpm, feed rate of 0.1 mm/rev, and average cutting speed of 35.28 m/min. The depth of cut was inherently variable

due to the geometry of the parting-off operation; however, since all tests were performed under identical cutting conditions, its influence is considered systematic and does not compromise the comparative analysis [14,19].

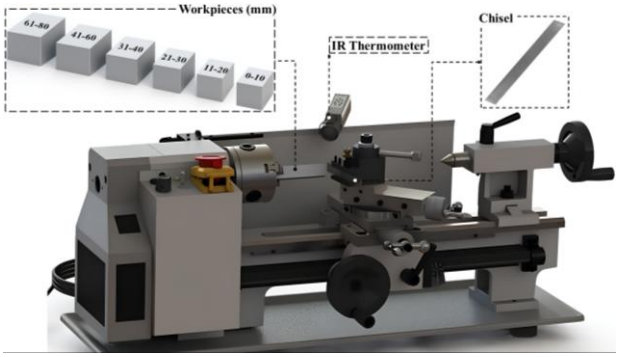

Fig. 2. Schematic representation of the cut-off (parting-off turning) operation and the divisions of the workpiece.

Machining was carried out at predefined positions along the solidification direction (10, 20, 30, 40, 60, and 80 mm from the cooled surface), allowing direct correlation between local thermal parameters, macrostructure, and machining response [14,19].

It is important to emphasize that machining tests were not repeated at each position. Due to the destructive nature of the experiment and the high cost associated with producing directionally solidified ingots under controlled conditions, a single cutting operation was performed per position. Consequently, the methodology is designed to establish physically consistent comparative trends rather than absolute machinability limits.

2.5 Surface roughness measurement and data treatment

Surface roughness evaluation was based on the average roughness parameter, adopted as the primary machinability criterion in this study. A conventional contact profilometer was not employed due to the severe nature of the parting-off operation. This machining process generates irregular and highly depressed surface features, preventing proper stylus contact, as the probe tip is unable to reach the deepest valleys of the rough surface.

Therefore, a non-contact optical method was adopted, which is widely reported in the literature for roughness evaluation under similar conditions [14]. After each cutting operation, the machined surface was subdivided into four quadrants to maximize the usable measurement area (Fig. 3(a)). High-magnification images (calibrated using a certified millimetric standard prior to quantitative analysis) were acquired using a stereomicroscope and processed using ImageJ® software with validated topographic extraction routines (Fig. 3(b)) [14]. The images were acquired with a spatial resolution of 156 pixels/μm.

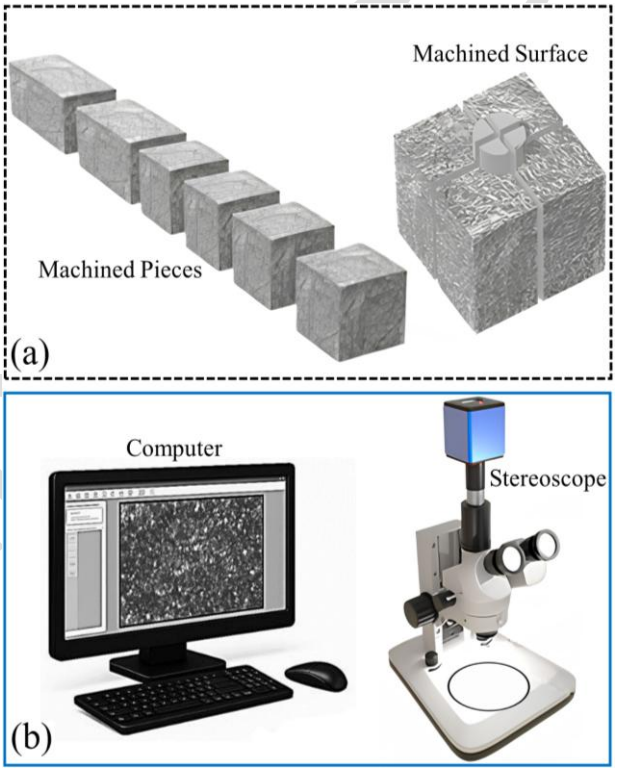

Fig. 3. (a) machined pieces and detail of the machined surface with quadrant division; (b) experimental setup for image acquisition, including the stereomicroscope and computer used for high-magnification image capture and subsequent quantitative analysis.

The Ra values reported correspond to the arithmetic mean obtained from multiple measurements extracted from different regions of the same machined surface. This approach allows statistical representation of surface roughness while accounting for local heterogeneities inherent to the machining process.

By correlating thermal parameters, macrostructural features, and surface roughness, this methodology provides a physically grounded framework for evaluating the machinability of Al-Sn alloys.

In the context of the present study, surface roughness, expressed by the Ra, was intentionally adopted as the single machinability metric. This choice reflects the objective of establishing a systematically comparable database, rather than providing a comprehensive evaluation of machinability in its broader sense.

Ra was selected because it represents an integrative surface descriptor, capturing the cumulative effects of material heterogeneity, chip formation instability, local plastic deformation, and phase pull-out phenomena that arise during machining of low-miscibility alloys. As such, Ra is particularly sensitive to variations in solidification-controlled macrostructure and solute distribution, making it suitable for correlation-based analyses.

In this framework, surface roughness is employed as an indirect proxy for surface integrity and tribological behavior, rather than as a complete descriptor of machinability. Variations in Ra reflect changes in near-surface deformation mechanisms, material smearing, and phase detachment, all of which are closely associated with frictional response and contact conditions in service. Therefore, while Ra does not exhaustively characterize machining performance, it provides a physically meaningful link between solidification-controlled microstructure and tribological-relevant surface features.

2.6 Methodological limitations and scope of the analysis

The machinability assessment conducted in this study is subject to methodological constraints that must be explicitly acknowledged to ensure proper interpretation of the results. Due to the destructive nature of the parting-off operation and the high experimental cost associated with producing directionally solidified ingots under controlled thermal conditions, machining tests were performed without repetition, with a single cut conducted at each evaluated position along the ingot length. Consequently, statistical dispersion metrics such as standard deviation or error bars are not reported.

This limitation implies that the present study does not aim to provide statistically convergent or probabilistic machinability values. Instead, the experimental design prioritizes spatially resolved measurements under strictly identical solidification and machining conditions, enabling the identification of physically consistent comparative trends along the ingot length.

The reliability of these trends is supported by the systematic variation of surface roughness, the consistency of the correlations with thermal solidification parameters (V_L and $\dot{T}$), and their agreement with well-established solidification-microstructure relationships reported in the literature. Therefore, the results should be interpreted as trend-based indicators rather than absolute or statistically bounded machinability metrics.

Within this framework, Ra was intentionally adopted as the sole machinability criterion. This choice reflects the objective of establishing a systematically comparable link between solidification parameters, macrostructural morphology, and machining response, rather than providing a comprehensive or statistically exhaustive evaluation of machinability.

3. RESULTS AND DISCUSSION

3.1 Thermal solidification parameters and macrostructural evolution

The directional solidification of the Al-10wt.%Sn and Al-20wt.%Sn alloys under transient heat extraction conditions resulted in distinct macrostructural morphologies along the length of the ingots. The thermal parameters, expressed in terms of the V_L and $\dot{T}$, decreased monotonically with increasing distance from the cooled mold surface, reflecting the progressive increase in thermal resistance imposed by the growing solidified layer [18,19]

Fig. 4(a), for the Al-10wt.%Sn alloy, the macrostructure exhibited a well-defined sequence of columnar, plumose (feathery), and equiaxed grain regions. Near the mold interface, high values of V_L and $\dot{T}$ favored stable columnar growth aligned with the heat flux direction. As solidification progressed, the reduction in thermal gradients combined with solute enrichment in the liquid promoted constitutional undercooling and interface destabilization, leading to the formation of plumose grains. At larger distances, further reductions in V_L and $\dot{T}$

enabled widespread nucleation ahead of the solid-liquid interface, resulting in an equiaxed grain structure [18].

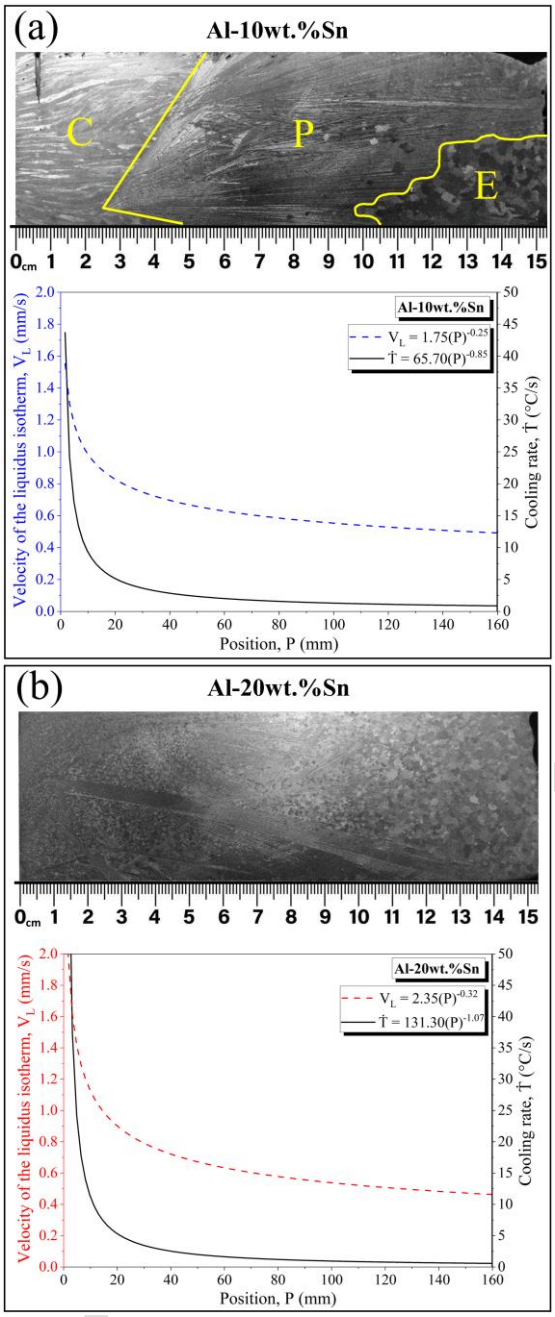

Fig. 4. Correlation of thermal parameters (V_L and $\dot{T}$) with the macrostructure zones of: (a) Al-10wt.%Sn and (b) Al-20wt.%Sn alloys.

In contrast, Fig. 4(b) the Al-20wt.%Sn alloy displayed a markedly different macrostructural behavior. Under the same thermal extraction conditions [19], the higher Sn content intensified constitutional undercooling and solutal convection effects, suppressing the formation of an extended columnar zone. As a result, the macrostructure was predominantly equiaxed from the early stages of solidification, with dispersed regions of plumose grains originating from multiple nucleation sites along the ingot.

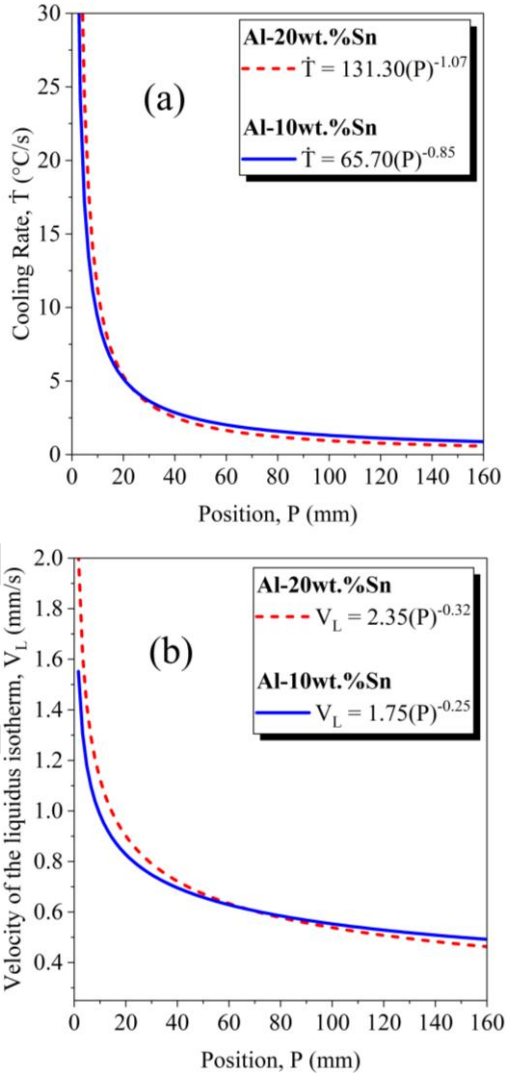

Fig. 5. (a) cooling rates and; (b) *liquidus* isotherm velocity of Al-10wt.%Sn and Al-20wt.%Sn alloys.

These observations align with previous studies on directionally solidified Al-Sn alloys, which show that increasing Sn content intensifies interface instability and promotes grain refinement via solute buildup ahead of the solidification front. Accordingly, solute concentration plays a decisive role in macrostructural selection, even under identical thermal boundary conditions [22,23]. Fig. 5 show the cooling rates and liquidus velocities of the Al-10wt.%Sn and Al-20wt.%Sn alloys, as observed for $\dot{T}$, V_L decreases progressively with the advancement of solidification, maintaining the typical behavior of transient processes. However, the Al-20wt.%Sn alloy exhibits higher isothermal displacement speeds than the Al-10wt.%Sn alloy throughout the entire evaluated range.

3.2 Role of tin content and thermal parameters in surface roughness

The comparison between the Al-10wt.%Sn and Al-20wt.%Sn alloys highlight the dual role of tin content in governing both solidification behavior and machining response. Increasing Sn content intensifies solute segregation during solidification, increasing constitutional undercooling and modifying the stability of the solidification front. This effect alters the evolution of V_L and $\dot{T}$ along the ingot and directly impacts macrostructural morphology.

From a machining perspective, higher Sn content introduces a greater volume fraction of soft, Sn-rich regions within the aluminum matrix. These regions act as solid lubricants during cutting, facilitating chip segmentation and reducing friction at the tool-workpiece interface. However, the beneficial effect of Sn is strongly modulated by its spatial distribution. In regions where Sn-rich phases are heterogeneously distributed, such as in plumose grain zones, the local mechanical contrast between phases can amplify surface irregularities.

The present results demonstrate that surface roughness is not governed solely by Sn content, but by the interaction between solute concentration, thermal solidification parameters, and the resulting macrostructure. Regions solidified under higher V_L and $\dot{T}$, which favor equiaxial grain formation, exhibit improved surface finish regardless of Sn content, while structurally unstable regions consistently lead to increased roughness.

Although tin-rich phases are widely recognized for their lubricating role, the present results indicate that excessive Sn content may generate surface topographies that are less favorable from a tribological standpoint. Increased roughness implies higher asperity interaction and non-uniform contact conditions, which can offset the beneficial effects of solid-state lubrication during sliding.

This observation highlights that tribological performance is not governed solely by the presence of lubricating phases, but also by the surface morphology inherited from the manufacturing route. Fig. 6 below shows the roughness values of the Al-10wt.%Sn and Al-20wt.%Sn alloys in each sample.

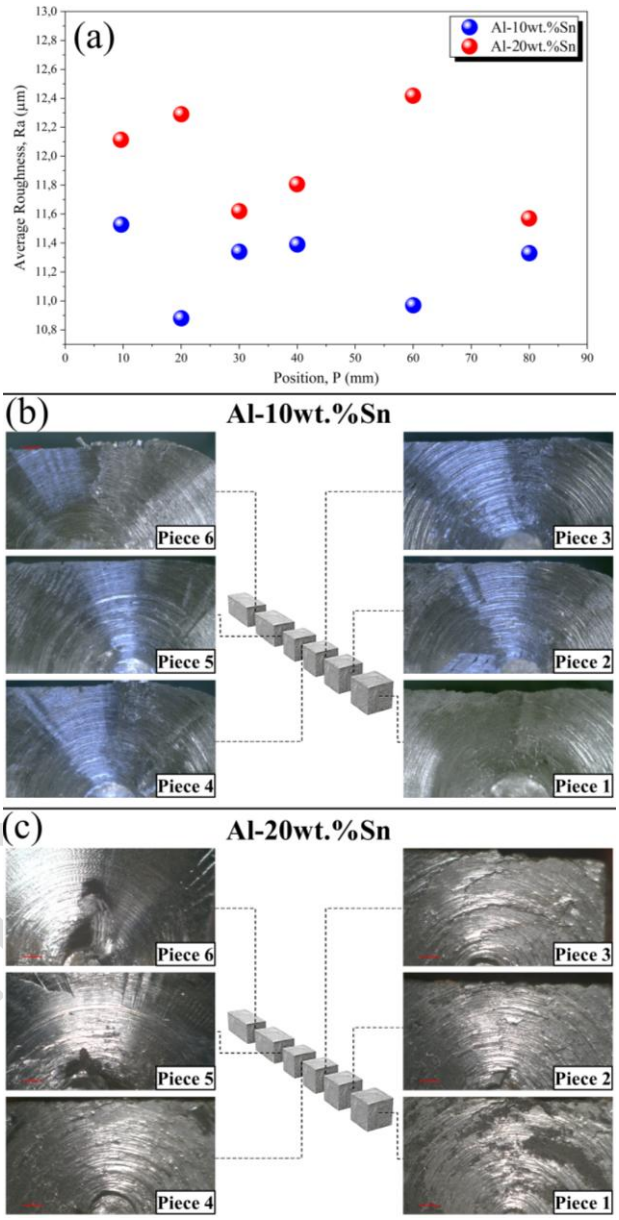

Fig. 6. (a) variation of Ra as a function of position along the length of the ingot for the alloys; Machined surface topographies of samples of (b) Al-10wt.%Sn and (c) Al-20wt.%Sn; extracted from different positions along the length of the ingot (Parts 1-6).

The Al-20wt.%Sn alloy shows slightly higher values in almost all positions. The highest average values are observed at P = 20 mm (Ra ≈ 12.3 μm) and P = 60 mm (Ra ≈ 12.4 μm). On the other hand, the Al-10wt.%Sn alloy has the lowest values recorded, especially at P = 20 mm (Ra ≈ 10.9 μm).

3.3 Influence of macrostructure on machining response

The machining behavior of the directionally solidified alloys was strongly dependent on the local macrostructural morphology established

during solidification [14,19,24]. Surface roughness, expressed by the Ra, exhibited systematic variations along the ingot length, reflecting the combined influence of thermal parameters and grain structure.

From a contact mechanics standpoint, the surface roughness generated during machining governs the initial interaction between the component and its counterface. Variations in Ra reflect changes in asperity density, height distribution, and local load-bearing capacity, which directly influence friction coefficients and wear initiation during sliding contact.

In Al-Sn alloys, this effect is further amplified by the presence of soft Sn-rich phases, which tend to smear or detach during machining. Such mechanisms alter the near-surface topography and, consequently, the tribological response under service conditions. As a result, the machining-induced roughness becomes a critical link between solidification-controlled macrostructure and tribological behavior.

These variations are clearly illustrated in Figs. 7 and 8, which correlates the evolution of surface roughness with the macrostructural zones along the ingot length.

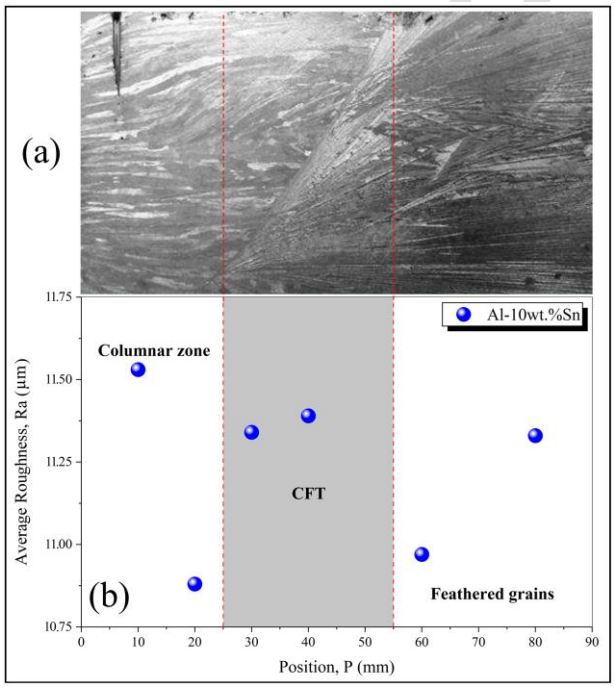

Fig. 7. (a) macrostructural image of the Al-10wt.%Sn alloy; (b) variation of Ra as a function of position along the ingot length for the Al-10wt.%Sn alloy under identical machining conditions.

Figs. 7(a) and 7(b), for the Al-10wt.%Sn alloy, higher Ra values were observed in regions corresponding to columnar and plumose grain morphologies, while lower roughness values were associated with equiaxial regions. The transition zones, particularly the columnar-to-plumose transition, exhibited the highest roughness levels. These regions are characterized by pronounced structural heterogeneity, anisotropic grain orientations, and complex interdendritic Sn distribution, which collectively promote unstable chip formation and local fluctuations in cutting forces.

Plumose zones exhibited the highest roughness due to the combined effects of strong morphological anisotropy, inclined surface features, mechanical heterogeneity, and unstable chip formation. Roughness measurements in plumose joints demonstrate scale-dependent anisotropy, with height distribution and correlation length varying with direction [25]. This directional variability causes fluctuating tool engagement and direction-dependent cutting forces, as commonly reported for anisotropic materials [26-29].

Unlike smoother mode-I tensile fractures, which form under low mean stress and exhibit lower topographic amplitude, plumose structures develop under higher mean stress and are associated with dilatancy and localized damage [30]. Their inclined “arms” locally modify the effective cutting geometry, promoting ploughing and intermittent micro-fracture. In multiphase Al-Sn alloys, hardness contrasts further aggravate this behavior: soft Sn-rich regions are susceptible to pull-out, while harder matrix or intermetallic areas increase force oscillation. Such heterogeneity favors non-uniform chip formation and surface tearing, mechanisms known to increase roughness [31,32,27,28].

Therefore, the worst roughness in plumose zones results from the coupling between directional surface anisotropy, locally inclined features, mechanical contrast, and chip instability, which together destabilize material removal and amplify surface irregularities.

Plumose grains are formed by twinned dendritic growth and exhibit inclined primary and secondary arms relative to the cutting direction [14,19]. This morphology introduces

anisotropy in mechanical response and disrupts uniform plastic flow during machining. Therefore, localized variations in shear resistance and heat dissipation occur at the tool-workpiece interface [19], leading to inferior surface finish. As shown in Fig. 7(a), growth is initially columnar, predominating up to approximately 25 mm from the metal/mold interface. Subsequently, an extensive region of feathery grains develops, with a well-defined columnar-to-feathery transition (CFT) in the range of 25 to 55 mm.

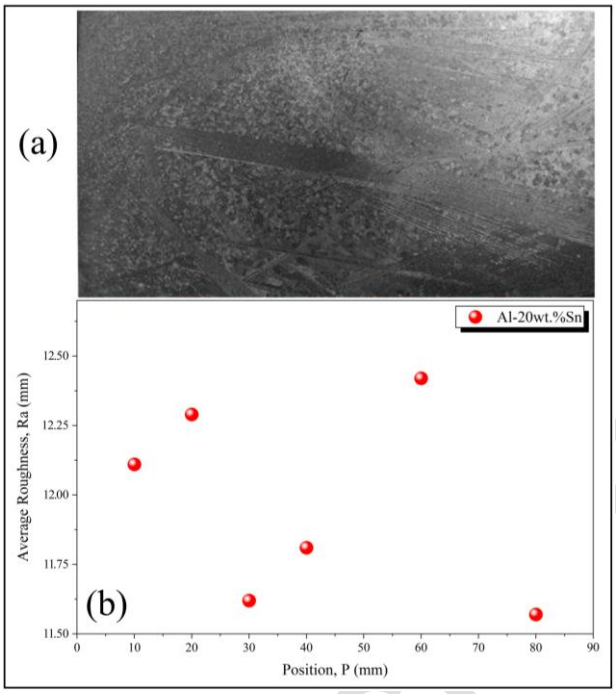

Fig. 8. (a) macrostructural image of the Al-20wt.%Sn alloy; (b) variation of Ra as a function of position along the ingot length for the Al-20wt.%Sn alloy under identical machining conditions.

In the Al-20wt.%Sn alloy, the predominance of equiaxial grains resulted in more homogeneous machining behavior along most of the ingot. This macrostructural configuration is shown in Figs. 8(a) and 8(b), where equiaxial grains predominate throughout nearly the entire ingot, with only localized regions of feathery grains.

The refined and isotropic grain structure facilitated more stable chip formation and distributed deformation more uniformly during cutting, which is reflected in comparatively lower and more consistent Ra values [19]. Although plumose grains were still present in localized regions, their dispersed nature limited their detrimental influence on surface quality.

These results are consistent, indicating that equiaxial microstructures enhance machining performance, whereas heterogeneous macrostructures impair surface integrity [14,19]. As observed in Fig. 8(a), under the same thermal and mold finishing conditions, equiaxed grains predominate throughout virtually the entire ingot, with multiple nucleation points of feathery grains distributed along the structure.

To facilitate an integrated comparison between thermal solidification parameters, macrostructural morphology, and machining response, Tabs. 1 and 2 summarizes representative values of $\dot{T}$, V_L, macrostructure, and Ra for both Al-10wt.%Sn and Al-20wt.%Sn alloys at selected positions along the ingot length.

Table 1. Summary of solidification parameters, macrostructure, and surface roughness at positions along the length of the Al-10wt.%Sn alloy ingot.

Al-10wt.%Sn				
P (mm)	**$\dot{T}$ (°C/s)**	**V_L (mm/s)**	**Macrostructural morphology**	**Ra (μm)**
10	9.28	0.98	Columnar zone	11.53
20	5.15	0.83	Columnar zone	10.88
30	3.65	0.75	CFT	11.34
40	2.86	0.70	CFT	11.39
60	2.36	0.66	Feathered grains	10.97
80	2.02	0.63	Feathered grains	11.33

Table 2. Summary of solidification parameters, macrostructure, and surface roughness at positions along the length of the Al-20wt.%Sn alloy ingot.

Al-20wt.%Sn				
P (mm)	**$\dot{T}$ (°C/s)**	**V_L (mm/s)**	**Macrostructural morphology**	**Ra (μm)**
10	11.18	1.13	Equiaxed -plumose	12.11
20	5.32	0.90	Equiaxed -plumose	12.29
30	3.45	0.79	Equiaxed -plumose	11.62
40	2.54	0.72	Equiaxed -plumose	11.81
60	2.00	0.67	Equiaxed -plumose	12.42
80	1.64	0.63	Equiaxed -plumose	11.57

3.4 Implications for machinability modeling and database development

The correlations established between V_L, $\dot{T}$, macrostructural morphology, and surface roughness provide a physically grounded basis

for interpreting the machinability of Al-Sn alloys. Rather than being an intrinsic material property, machining response is shown to arise from the combined effects of solidification history and resulting macrostructural architecture.

By maintaining identical solidification and machining conditions for both alloy compositions, the present approach enables direct comparison between datasets and supports the development of a structured machinability database. Such a framework allows predictive assessment of machining behavior based on solidification control, reducing reliance on empirical trial-and-error strategies for low-miscibility alloy systems.

3.5 Scientific and industrial implications

The results demonstrate that machinability in Al-Sn alloys is governed primarily by solidification history rather than alloy composition alone. The explicit correlation between thermal parameters (V_L and $\dot{T}$), macrostructural morphology, and surface roughness provides experimental evidence that machining performance can be systematically tailored through controlled solidification.

From a scientific perspective, these findings reinforce the concept of machinability as an emergent property resulting from interactions between solute redistribution, interface stability, and deformation mechanisms during cutting. The inferior surface integrity observed in plumose and heterogeneous macrostructures highlights the critical role of macrostructural heterogeneity in machining behavior [14,33].

From an industrial standpoint, linking machining quality to solidification parameters enables process optimization at the casting stage, minimizing the need for post-processing adjustments. Promoting refined equiaxial macrostructures through solidification control offers a practical pathway to improve surface finish and machining reliability in cast Al-Sn components.

4. CONCLUSIONS

Based on the experimental results and integrated analysis of the study, the following conclusions are summarized as follows:

1. Directional solidification under transient heat extraction produced distinct macrostructural morphologies in the Al-10wt.%Sn and Al-20wt.%Sn alloys, even under identical thermal boundary conditions. While the Al-10wt.%Sn alloy exhibited a sequence of columnar, plumose, and equiaxial grains, the higher Sn content intensified constitutional undercooling, leading to a predominantly equiaxial macrostructure with dispersed plumose regions.
2. V_L and $\dot{T}$ played a decisive role in macrostructural selection. Higher values favored equiaxial grain formation, whereas reductions in these parameters promoted structural heterogeneity and the development of plumose morphologies.
3. Machining response, assessed through Ra, was strongly governed by local macrostructural morphology. Regions containing plumose grains or macrostructural transition zones exhibited higher roughness due to unstable chip formation and non-uniform deformation during cutting.
4. Although Sn-rich phases contribute to self-lubricating behavior, improved and more homogeneous surface finish was achieved primarily in regions with favorable and homogeneous macrostructures, indicating that grain morphology plays a dominant role in stabilizing machining response.
5. The comparison between Al-10wt.%Sn and Al-20wt.%Sn alloys demonstrates that machinability is governed by the coupled interaction between alloy composition, thermal solidification parameters, and resulting macrostructure, rather than by solute content alone.
6. From a tribological perspective, surface roughness can be regarded as an intermediate variable linking solidification history to potential in-service contact behavior, as it influences asperity interaction, real contact area, and lubricant retention. Accordingly, control of solidification parameters may contribute not only to tailoring machinability, but also to indirectly affecting tribological performance.

Overall, while the present framework does not aim to establish absolute machinability limits, it provides a physically consistent basis for

microstructure-driven correlations and for the development of machinability databases grounded in controlled solidification conditions.

Acknowledgement

The authors would like to express their gratitude for the financial support granted by the National Council for Scientific and Technological Development (CNPq) and the Coordination for the Improvement of Higher Education Personnel (CAPES), Brazil. We also thank the Federal University of Pará (UFPA) and the Federal Institute of Pará (IFPA) for the research infrastructure, laboratory facilities, and institutional support that made this work possible.

REFERENCES

[1] Z. Zeng, Y. Li, H. Wang, R. Lai, J. Teng, and Y. Li, "Tribological behavior of AlSn20Cu alloy manufactured by additive friction stir deposition," *Wear*, vol. 560, p. 205606, 2025, doi: 10.1016/j.wear.2024.205606.

[2] N. M. Rusin, A. L. Skorentsev, and A. I. Dmitriev, "Contribution of tin to the strain hardening of self-lubricating sintered Al-30Sn alloy and its wear resistance under dry friction," *Materials*, vol. 16, no. 4, p. 1356, 2023, doi: 10.3390/ma16041356.

[3] K. H. Kim, M. A. Slazhniev, S. W. Kim, H. S. Sim, and K. Euh, "Study on controlled segregation of Al-Sn alloys for bearings," in *8th International Conference on Electromagnetic Processing of Materials*, Oct. 2015.

[4] C. Confalonieri, R. Casati, and E. Gariboldi, "Effect of process parameters on laser powder bed fusion of Al-Sn miscibility gap alloy," *Quantum Beam Science*, vol. 6, no. 2, p. 17, 2022, doi: 10.3390/qubs6020017.

[5] P. Bassani, M. Molteni, and E. Gariboldi, "Microstructural features and thermal response of granulated Al and A356 alloy with relevant Sn additions," *Materials & Design*, vol. 229, p. 111879, 2023, doi: 10.1016/j.matdes.2023.111879.

[6] R. Oliveira, C. Cruz, A. Barros, F. Bertelli, J. E. Spinelli, A. Garcia, and N. Cheung, "Thermal conductance at Sn-0.5 mass% Al solder alloy/substrate interface as a factor for tailoring cellular/dendritic growth," *Journal of Thermal Analysis and Calorimetry*, vol. 147, no. 8, pp. 4945-4958, 2022, doi: 10.1007/s10973-021-10755-w.

[7] X. Ao, H. Xia, J. Liu, Q. He, and S. Lin, "A numerical study of dendrite growth and microstructure transition in a non-equilibrium solidification," in *Journal of Physics: Conference Series*, vol. 1939, no. 1, May 2021, p. 012018.

[8] R. Septimio, C. A. Silva, T. A. Costa, A. Garcia, and N. Cheung, "Hypereutectic Zn-Al alloys: microstructural development under unsteady-state solidification conditions, eutectic coupled zone and hardness," *Metals*, vol. 12, no. 7, p. 1076, 2022, doi: 10.3390/met12071076.

[9] G. Reinhart, F. Ngomesse, F. Bertelli, P. Benigni, A. Campos, and H. Nguyen-Thi, "Investigation of Al-20Sn-10Cu alloy directional solidification by laboratory X-radiography," in *IOP Conference Series: Materials Science and Engineering*, vol. 1274, no. 1, 2023, p. 012054, doi: 10.1088/1757-899x/1274/1/012054.

[10] J. Cao, Z. Zeng, F. Zhang, D. Guo, and Z. Hou, "Effect of cooling rates on the local-overall morphology characteristics of solidification structure at different stages for high carbon steel," *Metals*, vol. 11, no. 8, p. 1291, 2021, doi: 10.3390/met11081291.

[11] M. Ulas, O. Aydur, T. Gurgenc, and C. Ozel, "Surface roughness prediction of machined aluminum alloy with wire electrical discharge machining by different machine learning algorithms," *Journal of Materials Research and Technology*, vol. 9, no. 6, pp. 12512-12524, 2020, doi: 10.1016/j.jmrt.2020.08.098.

[12] U. Sajjad, A. Abbas, A. Sadeghianjahromi, N. Abbas, J. S. Liaw, and C. C. Wang, "Enhancing corrosion resistance of Al 5050 alloy based on surface roughness and its fabrication methods; an experimental investigation," *Journal of Materials Research and Technology*, vol. 11, pp. 1859-1867, 2021, doi: 10.1016/j.jmrt.2021.01.096.

[13] Y. Zedan, A. M. Samuel, H. W. Doty, V. Songmene, and F. H. Samuel, "Effects of trace elements on the microstructural and machinability characteristics of Al-Si-Cu-Mg castings," *Materials*, vol. 15, no. 1, p. 377, 2022, doi: 10.3390/ma15010377.

[14] T. I. M. Botelho, A. C. da C. Maciel, F. S. da Rocha, and J. M. Nascimento, "Correlação entre rugosidade superficial e estrutura da solidificação direcional horizontal de uma liga Al-10%Sn," *Cuadernos de Educación y Desarrollo*, vol. 15, no. 2, pp. 1600-1610, 2023, doi: 10.55905/cuadv15n2-031.

[15] C. E. Cross, "Applying solidification theory to aluminum weldability and consumable development," *Welding Journal*, vol. 101, 2022, doi: 10.29391/2022.101.016.

[16] D. Y. Pimenov, M. Kiran, N. Khanna, G. Pintaude, M. C. Vasco, L. R. R. da Silva, and K. Giasin, "Review of improvement of machinability and surface integrity in machining on aluminum alloys," *The International Journal of Advanced Manufacturing Technology*, vol. 129, no. 11, pp. 4743-4779, 2023, doi: 10.1007/s00170-023-12630-4.

[17] S. L. Paula, J. M. S. Dias Filho, C. F. Santos, T. A. P. Sousa Costa, and O. F. L. Rocha, "Usinabilidade de uma liga Al-6% Cu solidificada em um dispositivo direcional horizontal, pelo critério de temperatura de corte," *Brazilian Journal of Development*, vol. 7, no. 6, pp. 60959-60971, 2021, doi: 10.34117/bjdv7n6-460.

[18] J. M. Nascimento, I. A. B. Magno, A. D. S. Barros, A. D. J. Vasconcelos, O. F. L. Rocha, and M. A. P. S. Silva, "Análise macroestrutural de uma liga Al-10%Sn solidificada em um dispositivo direcional horizontal refrigerado a água," in *Ciência e Engenharia de Materiais: Conceitos, Fundamentos e Aplicação*, cap. 6, pp. 81-89, 2021, doi: 10.37885/210404241.

[19] A. I. C. Holanda, A. C. C. Maciel, J. M. Nascimento, G. A. Gomes, H. R. O. Souza, T. A. P. S. Costa, and A. P. Silva, "The role of thermal and microstructural parameters for machinability optimization of Al-20 wt.%Sn alloy," in *28th ABCM International Congress of Mechanical Engineering*, Curitiba, Brazil, 2025, vol. 1.

[20] ASTM E3-11(2017)e1, *Standard Guide for Preparation of Metallographic Specimens*, ASTM International, 2017.

[21] F. Rocha, "Analysis of metallurgical conditions favorable to machinability of an A413.0 alloy series: Cutting temperature criteria," in *Congresso Brasileiro de Engenharia e Ciência dos Materiais*, 2022.

[22] K. S. Cruz, J. E. Spinelli, I. L. Ferreira, N. Cheung, and A. Garcia, "Microstructural development in Al-Sn alloys directionally solidified under transient heat flow conditions," *Materials Chemistry and Physics*, vol. 109, no. 1, pp. 87-98, 2008, doi: 10.1016/j.matchemphys.2007.10.037.

[23] A. de J. Vasconcelos, C. V. A. da Silva, A. L. S. Moreira, M. A. P. de S. da Silva, and O. F. L. da Rocha, "Influence of thermal parameters on the dendritic arm spacing and the microhardness of Al-5.5 wt.%Sn alloy directionally solidified," *REM: Revista Escola de Minas*, vol. 67, no. 2, pp. 173-179, Apr. 2014, doi: 10.1590/S0370-44672014000200007.

[24] A. P. Silva, I. R. Prado, J. S. Barros, C. A. P. Silva, A. L. Moreira, and O. L. Rocha, "Analysis of the cutting temperatures along the macrostructure of a directionally solidified Al-7 wt.% Si alloy," in *Defect and Diffusion Forum*, vol. 365, Aug. 2015, pp. 116-121.

[25] B. Nigon, A. Englert, C. Pascal, and A. Saintot, "Multiscale characterization of joint surface roughness," *Journal of Geophysical Research: Solid Earth*, vol. 122, no. 12, pp. 9714-9728, 2017, doi: 10.1002/2017jb014322.

[26] S. Tian, Z. Wang, Z. Wang, K. Luo, and J. Lu, "The mechanism of anisotropic micro-milling properties in additively manufactured Ti-6Al-4V alloy," *Journal of Materials Processing Technology*, vol. 322, p. 118190, 2023, doi: 10.1016/j.jmatprotec.2023.118190.

[27] W. Huang and J. Yan, "Surface formation mechanism in ultraprecision diamond turning of coarse-grained polycrystalline ZnSe," *International Journal of Machine Tools and Manufacture*, vol. 153, p. 103554, 2020, doi: 10.1016/j.ijmachtools.2020.103554.

[28] Ş. Ötenkaya and R. Ünal, "Effect of surface/subsurface defects on the surface integrity of ceramic materials," *Journal of the Korean Ceramic Society*, vol. 62, no. 3, pp. 412-436, 2025, doi: 10.1007/s43207-025-00501-5.

[29] C. Ni, L. Zhu, Z. Zheng, J. Zhang, Y. Yang, J. Yang, and H. Wang, "Effect of material anisotropy on ultra-precision machining of Ti-6Al-4V alloy fabricated by selective laser melting," *Journal of Alloys and Compounds*, vol. 848, p. 156457, 2020, doi: 10.1016/j.jallcom.2020.156457.

[30] A. I. Chemenda, S. H. Nguyen, J. P. Petit, and J. Ambre, "Mode I cracking versus dilatancy banding: Experimental constraints on the mechanisms of extension fracturing," *Journal of Geophysical Research: Solid Earth*, vol. 116, no. B4, 2011, doi: 10.1029/2010jb008104.

[31] Z. Xue, M. Lai, F. Xu, and F. Fang, "Influence factors and prediction model of surface roughness in single-point diamond turning of polycrystalline soft metal," *Journal of Materials Processing Technology*, vol. 324, p. 118256, 2024, doi: 10.1016/j.jmatprotec.2023.118256.

[32] Z. Sun, S. To, S. Zhang, and G. Zhang, "Theoretical and experimental investigation into non-uniformity of surface generation in micro-milling," *International Journal of Mechanical Sciences*, vol. 140, pp. 313-324, 2018, doi: 10.1016/j.ijmecsci.2018.03.019.

[33] E. S. Freitas, A. P. Silva, J. E. Spinelli, L. C. Casteletti, and A. Garcia, "Inter-relation of microstructural features and dry sliding wear behavior of monotectic Al-Bi and Al-Pb alloys," *Tribology Letters*, vol. 55, no. 1, pp. 111-120, 2014, doi: 10.1007/s11249-014-0338-8.